

Enhanced Safety Performance of Automotive Lithium-Ion Batteries with Al_2O_3 -Coated Non-Woven Separator

Fanhui Meng,*^[a, b] Jinhui Gao,^[b] Mengdi Zhang,^[a] Dongwei Li,^[c] and Xizheng Liu*^[a]

Thermal runaway (TR) is the fatal safety defects that hinder the wide application of automotive batteries. The short circuit caused by shrinkage of separators under high temperatures leads to TR. In this paper, we demonstrate the robust thermal stability of an Al_2O_3 coated non-woven polyethylene terephthalate (PET) separator. The shrinkage ratio of the Al_2O_3 coated separator has been compared with the non-coated polyethylene (PE) separator by differential scanning calorimetry (DSC), thermogravimetry (TG) and heat nail tests. Automotive

lithium-ion batteries (LIBs) with large capacities have been used to conduct the simulations of nail penetration. TR is found to be triggered by Joule heat generation during the shrinkage of the separators. The separator with lower shrinkage retains highly stable dimension against wide range temperature changes. This feature enables the Al_2O_3 coated separator to prevent inner short circuits. The improved safety performance indicates a promising prospect of Al_2O_3 coated non-woven separators in LIBs.

1. Introduction

The need of lithium-ion batteries (LIBs) with high energy and power density is increasing rapidly with the development of electric vehicles. The safety performance is one of the most important concerns for the users of automotive LIBs. Separator is the important component of the LIBs that separates the cathodes and anodes to avoid short-circuit.^[1–6] The composition and structure of separators greatly influence the internal resistance and safety performance of LIBs.^[7–13] They are drawing increasing attentions as many researches about separators have been done to meet the safety requirements of the LIBs.^[14–19] Furthermore, separators possess another important function of storing liquid electrolyte within batteries. Separator shrinkage at high temperatures or the porosity shutdown leads to large area inner short circuit in the cell. The internal short circuit is to blame for the chain reactions among the cell components, including anodes, cathodes, electrolytes and separators, which lead to the tremendous heat release. Therefore, high mechanical strength, robust thermal stability and also low internal resistance are the key requirements of advanced separators for high-performance LIBs.^[20–27]

[a] Dr. F. Meng, M. Zhang, Prof. X. Liu

Tianjin Key Laboratory of Advanced Functional Porous Materials,
Institute for New Energy Materials and Low-Carbon Technologies,
School of Materials Science and Engineering
Tianjin University of Technology
Tianjin, 300384, P. R. China
E-mail: mengfanhui@lishen.com.cn
xzliu@tjut.edu.cn

[b] Dr. F. Meng, J. Gao

Tianjin Lishen Battery Joint-Stock Co. Ltd.
Huayuan High-Tech Industry Park,
Tianjin, 300384, P. R. China

[c] Dr. D. Li

Advanced Materials Institute
Qilu University of Technology (Shandong Academy of Science)
Jinan, 250014, P. R. China

 Supporting information for this article is available on the WWW under
<https://doi.org/10.1002/batt.202000169>

The main commercial separators for LIBs are micro-porous polyolefin separators, including polypropylene (PP), PE, and the composite multilayer polymer separators. Unfortunately, the thermal shrinkage ratio of single component polyolefin separators is quite high. Therefore, it is necessary to develop new types of single polymer or composite separators to fulfill the thermal stability requirements of LIBs.^[28–33] Ceramic-based composite separators are prepared to mitigate the performance-limitations of the conventionally used separator.^[34–39] Nonwoven fabric based separators with excellent thermal stability and higher electrolyte take-up are also getting more attentions recently.^[40–41] However, the TR mechanism in LIBs is still controversial in regard to the roles of anode and cathode.^[42]

To address the aforementioned mechanistic problem, we carried out the in-depth analysis on automotive pouch LIBs during the nail penetration process to clarify the TR mechanism. This study aims to investigate the thermal stability and failure mechanism of LIBs using Al_2O_3 modified non-woven separator and the PE separator with different melting temperatures. Simulation of nail penetration cells using separators with different shrinkage ratios are designed to detect and compare the internal short circuit resistances. The performances were studied by large-scale automotive cells with PET/ceramic non-woven separator and the PE separator.

2. Results and Discussion

The SEM images of PE and Al_2O_3 modified non-woven separators are presented in Figure 1. Figure 1a shows the interconnected spherical micro-pores with diameters of 100–300 nm in fibers web morphology. The average diameter of the fibers is about 100–200 nm. Figure 1b and 1c display the cross-section scanning electron microscope (SEM) images of the PE. The 20 μm -thick pure PE separator had a uniform multilayer porous structure with an interval of almost 100–200 nm, which

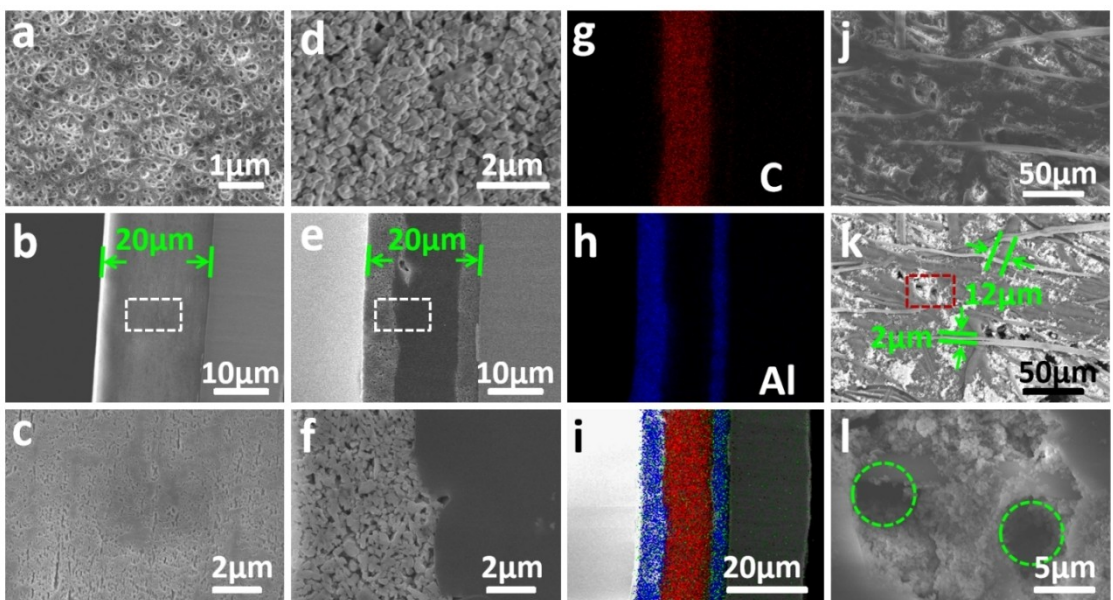


Figure 1. a) Top-view and b, c) cross-section SEM images of PE separator. d) Top-view and e, f) cross-section SEM images of PET separator. g, h) Elements distribution of C and Al. i) Composed plot of elements of C and Al. j) SEM and k) back-scattered SEM images of the substrate PET separator. The enlarged red rectangle in (k) is shown in (l).

is equal to the diameter of the PE fibers. In order to increase safety and cycle life of the battery, Al_2O_3 modified non-woven is always used as the mechanical substrate/matrix supporting ceramic particles, which fills the “open” structure and levels a rough surface of the separator. The as-obtained composite separator is Al_2O_3 modified non-woven separator. As shown in Figure 1d, the surface of the PET/ceramic non-woven separator is composed of sub-micro-scale inorganic particles. The cross-section in Figure 1e and 1f show that the PET non-woven separator was coated with the layers of sub-micro-scale ceramic particles on both the left and the right sides. Its cross-section was screened by SEM energy-dispersive spectrometer (SEM-EDS) mapping as displayed in Figure 1g and 1h. Carbon and Aluminum are marked as the red and blue points, which are composed as the one plot in Figure 1i. This image suggests the Al_2O_3 modified non-woven separator has a sandwich-like configuration. To completely study the separator’s structure, the PET separator substrate was prepared by peeling the Al_2O_3 layer off the Al_2O_3 modified non-woven separator. The SEM image and the back-scattered SEM image of the substrate of the PET separator are shown in Figure 1j and 1k, respectively. The pore size of the PET substrate separator is between 2–12 μm , which is composed of the PET fibers with an average diameter of 5–10 μm . Figure 1l shows the enlarged SEM image, where micro-scale pores without Al_2O_3 filling in the inner layer of the PET separator were observed. Such inner pores should be responsible for the high porosity, resulting in an excellent electrolyte holding performance. Detailed morphology can be found in Figure S1.

The thermal shrinking tests of the PE and Al_2O_3 modified non-woven separators with a 2-step temperature program. The temperature-time curve was shown in Figure 2a. As shown in Figure 2b and 2c, the shrinkage onset temperature is around

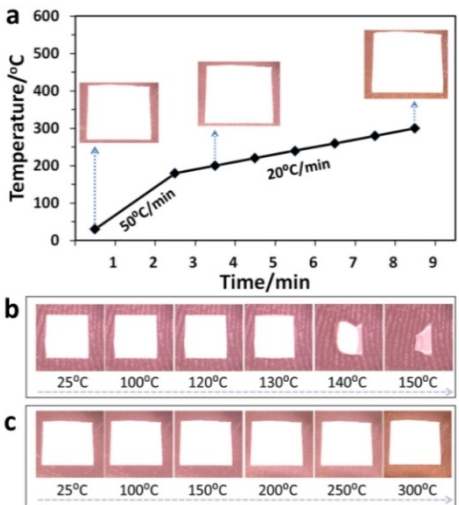


Figure 2. a) Shrinking tests of Al_2O_3 modified non-woven separators. Digital photos of b) PE- and c) Al_2O_3 -modified non-woven at different temperature.

130 °C for PE separator, in contrast, no shrinkage was observed for the Al_2O_3 modified non-woven separator even at 300 °C. Figure 3a and 3b show the TG and DSC analysis of the separators. TG results show that the mass losses happened at around 200 °C and completed at 500 °C for both the PE and Al_2O_3 modified non-woven separators. The mass losses of PE and Al_2O_3 modified non-woven separators reach 100% and 30% above 500 °C, attributed to the degradation of the polymer PE and PET. The lost mass confirms that the polymer content of PE and PET/ceramic non-woven separator are 100% and 30%, respectively. For the DSC analysis, the endothermic peak of the PE separator is located around 150 °C caused by the melting of PE. Two endothermic peaks of the PET/ceramic

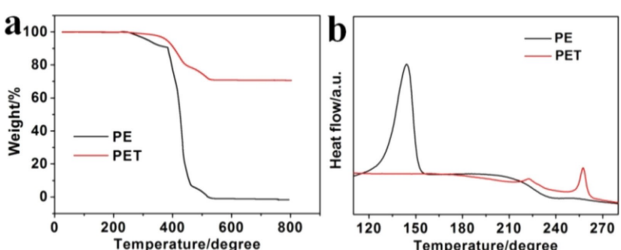


Figure 3. a) Thermogravimetries and b) differential scanning calorimetry of PE and PET separators.

non-woven separator appear around 225 and 255 °C, which are ascribed to the melting of the binder and PET^[36–38]. The DSC analysis reveals that the beginning melting temperature of the PET separator is 220 °C, which is much higher than that of the PE separator. Other detailed physical parameters have been determined, which are presented in supporting information.

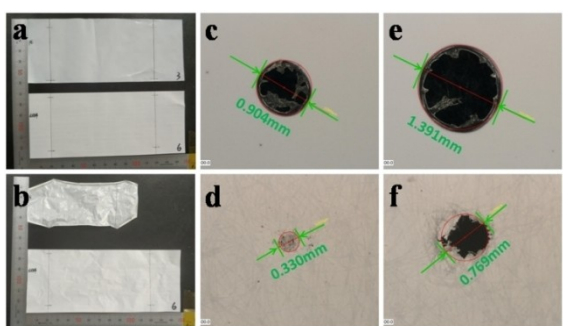


Figure 4. a, b) Photos of PE- and Al₂O₃-modified non-woven separators before and after the thermal shrinking tests. c, d) Thermal shrinking of PE- and Al₂O₃-modified non-woven separators under 200 °C nails. e, f) Thermal shrinking of PE and PET separators under 300 °C nails.

The contact angles of the electrolyte on PE and Al₂O₃-coated non-woven separator are shown in Figure S2. The contact angles of the electrolyte on the PE and the Al₂O₃-coated non-woven separator are 28.2° and 17.2°. The test suggests the electrolyte infiltration is improved for the Al₂O₃-coated non-woven separator. The well Mechanical parameters and comparison are listed in Table S1.

For a better view of the thermal stability of the two separators, the shrinking tests of large area separators were carried out. Photos of the two separators before and after heating are shown in Figure 3a and 3b. The shrinkage ratios of PE separator at 130 °C along transverse and machine direction are 16.7 and 26.7%, respectively. In contrast, no shrinkage was observed for the PET/ceramic non-woven separator. To further confirm the prior thermal stability of the Al₂O₃-modified non-woven, the hot nail tests were carried out, and the results are shown in Figure 4c, 4d, 4e and 4f. For the PE separator, holes with diameters of 0.904 and 1.391 mm formed in the 200 °C and 300 °C hot nail tests, respectively. Much smaller holes were observed in the Al₂O₃ modified non-woven separator, with diameters of 0.33 and 0.769 mm under the 200 °C and 300 °C hot nails, respectively.

In order to better understand the effect of the separator shrinkage to the safety of pouch LIBs, battery penetration simulations were carried out for both separators. The nail penetration simulation is presented in Figure 5a and nail penetration was conducted on a pouch cell without electrolyte under a constant voltage of 4.2 V. The cells were disassembled after the nail penetration and the photos are shown in Figure 5b and 5c. A hole with a diameter of 6 mm was observed in the PE separator, while a 3 mm diameter hole without any shrinkage was observed in the Al₂O₃-modified non-woven separator. The shrinkage of the PE separator was driven by the Joule heat generated during penetration. No shrinkage

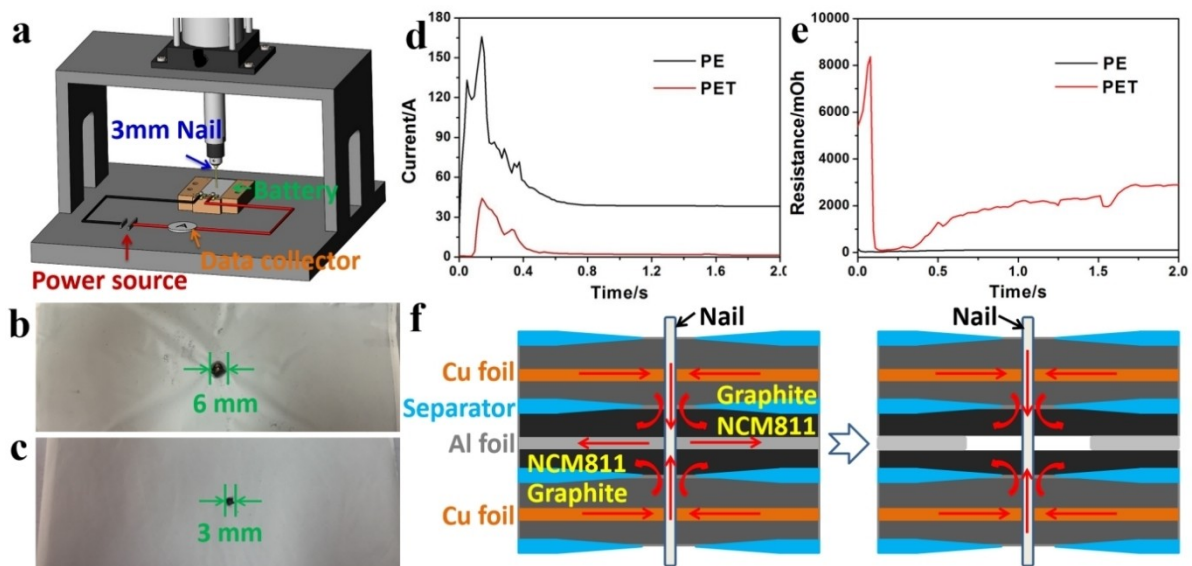


Figure 5. a) Scheme of nail penetration simulation. b, c) Photos of cells with PE- and Al₂O₃-modified non-woven separators after nail penetration simulating tests. d, e) Nail penetration simulating tests analysis under 4.2 V with different separators. f) Illustration of proposed short-circuit process in the nail penetration simulation.

happened on the Al_2O_3 -modified non-woven separator, which suggests the nail temperature was lower than the melting point of PET. To reveal the shrinkage effect of the separators during nail penetration simulation, the relationship of time and current was monitored and demonstrated in Figure 5d. According to the equation: $E = \int (V^2/R)dt$ (where E , V , R and t is the Joule heat, voltage, short-circuit resistance and time), larger currents are detected from the PE separator based battery, which suggests the cell with PE separator has a lower inner resistance and more Joule heat was generated during the nail penetration.

To better understand the effect of the separator shrinkage on the heat generation of the battery during nail penetration, the currents are transformed to the inner resistances according to the following equation: $R = V/I$, where I is the current recorded during the nail penetration simulation. Evolution of the inner resistance on the time is illustrated in the $R-t$ curves in Figure 5e. The internal short circuit resistance is related to the R_{nail} and R_{con} according to the equation: $R = R_{\text{nail}} + R_{\text{con}}$, where R_{nail} and R_{con} are the nail resistance and the contact resistance between the nail and the cell core. The schematic representation of the short circuit mechanism is shown in Figure 5f. The R_{nail} was influenced by the nail penetrating depth and the R_{con} is the deciding factor of the short circuit resistance. It is affected by not only the nail penetrating depth but also the inner physical/chemical processes. As shown in Figure 5d, a three-stage procedure of the time-dependent current was observed. In the first stage, the short circuit current increased exponentially to the peak value right after the cell core was penetrated through. The current rose largely as the contact area between the nail and the cell core increased. The current rising was caused by the separator melting. In the second stage, the current decreased largely from the peak value to the value close to the current platform at 0.6 s. In this stage, the Joule heat was high enough to melt the Aluminum collector, resulting in the increase of the contact resistance. The current decreased along with the melting of Aluminum collector until no contact existed between the nail and Al current collector. During the last stage after 0.6 s, the current decreased slowly, forming a current platform. In this stage, the current decreased with the cooling down of the cell. The three-stage procedure was also confirmed by the time-dependent short circuit resistance (Figure 5e).

It can be deduced from the simulation that the shrinkage of the separators correlates with the Joule heat generation. As proposed, higher melting point and mixing ceramic plays critical roles in the much lower shrinkage ratio under high temperatures for Al_2O_3 -modified non-woven separator. In terms of the safety performance of batteries, separators with higher thermal stability are promising for batteries with high capacity and power densities. For a deep investigation of the separators, the safety behaviors of the automotive batteries based on the PE and Al_2O_3 -modified non-woven separators were evaluated. Rate, direct current inner resistance (DCIR) and cycling performance of the automotive battery with the normal initial discharge capacity of the 42 Ah are shown in Figure 6. The discharging curves of the cells with the two different separators

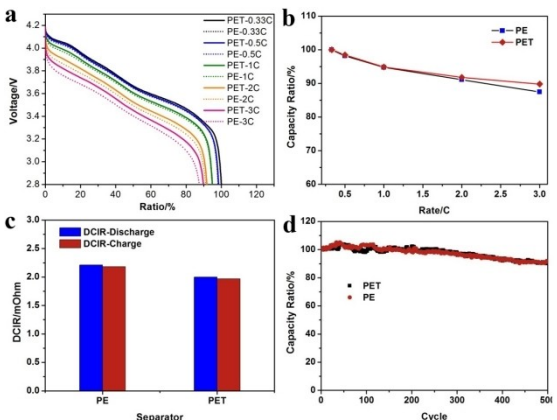


Figure 6. a) Discharging profiles of the cells at different rates. b) Dependence of capacity with discharge rate for the test cells. c) DCIR tests of the cells. d) Cycling performance of the cells.

are essentially same at various rates. The battery using Al_2O_3 -modified non-woven separator exhibited a better discharging performance especially at the higher rates for the higher porosity. The DCIR analysis for the two separators is demonstrated in Figure 6c, indicating a lower inner resistance for the battery with the Al_2O_3 -modified non-woven separator. Cycling tests were conducted, and the discharge capacity of the battery with the PE separator and Al_2O_3 -modified non-woven separator remained 90% and 91% after 500 cycles. There was no obvious difference in the cycling stability.

Nail penetration tests were performed on both of the pouch cells using the PE separator or the Al_2O_3 -modified non-woven separator. Dependence of voltage and temperature versus time during nail penetration tests are shown in Figure 7a. For the cell with PE separator, the puncture led to a

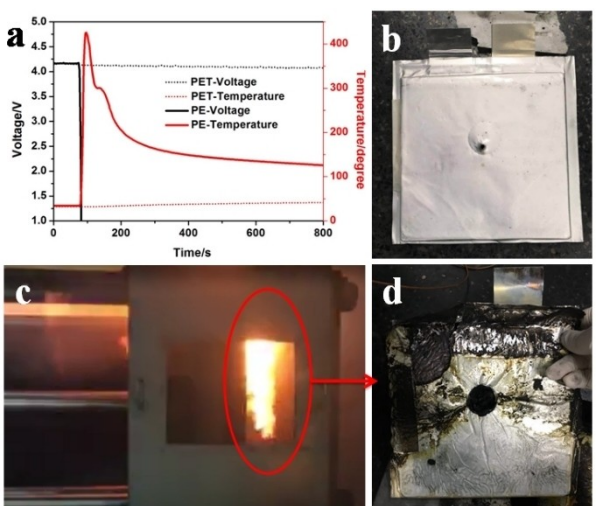


Figure 7. a) Dependences of voltage and temperature versus time during nail penetration tests for cells with the PE- and Al_2O_3 -modified non-woven separators. b) The cell with the PET separator after nail penetration. c) The cell with PE separator firing during nail penetration. d) The residual of cell with the PE.

rapid drop of the voltage to 0 V; for the cell with the Al_2O_3 -modified non-woven separator, a light decrease happened. A sharp increase of temperature caused by the pouch cell bursting was detected with a peak temperature of 425 °C for the cell with the PE separator. For the cell with the Al_2O_3 -modified non-woven separator, the temperature increased slowly from 30 to 50 °C in 2000 s, indicating a slight short circuit gave rise to a heat release rather than burning.

The pouch cells for nail penetration are shown in Figure 7b, 7c and 7d. For the cell with the Al_2O_3 -modified non-woven separator, no abrupt and energetic failure was observed with a hole punctured through the center of the cell body. The nail penetration test have been repeated for 3 times, and all of the cells with Al_2O_3 coated non-woven separator passed the test as shown in Figure S3. The photo of cathode of the cell with the Al_2O_3 coated non-woven separator after nail penetration is shown in Figure S4. It still keeps stable and unburned. The cell with the PE separator spouted flames as the exterior was punctured (Figure 7c). As a result of the abrupt temperature increase, no aluminum foil or aluminum tab was found in the residual of the burned cell and even the pouch shell was melted down. As mentioned in the nail penetration simulation, the short circuit between the nail and cell core caused by the separator shrinkage induces Joule heat generation, which results in the cell TR.

3. Conclusions

In conclusion, the separator plays a vital part in the protection of the cell from an internal short circuit before TR for the nail penetration test. Thermal stability test suggests that the substrates with higher melting points or the impregnation of the ceramic particles is beneficial to prevent the separators from shrinking at high temperatures. Simulation of nail penetration indicates that cells using separators with different shrinking ratios affect the internal short circuit resistances. The cell with the PET/ceramic non-woven separator exhibits lower DCIR and better discharging rate performance; as for the cycling performance, there is no difference between the PE separator and the Al_2O_3 -coated one. For the 42 Ah pouch cells with the same chemistry composition, the experimental results demonstrate that the separator with higher thermal stability performs much safer in the nail penetration. The results will help people understand the thermal behavior and how the separator shrinkage induces the inner short circuit of the lithium ion battery. It could be concluded that the safety behavior of automotive LIBs could be modified by the regulation of the separator properties. We hope that this work could help people better understand the mechanism of TR and shed light on the LIBs design in the future.

Experimental Section

Battery Fabrication

The automotive pouch cells were assembled in the laminated type with a capacity of 42 Ah. Lithium transition metal oxide $\text{LiNi}_{0.5}\text{Co}_{0.2}\text{Mn}_{0.3}\text{O}_2$ (NCM523) and graphite were used as cathode and anode, respectively. The traditional PE or Al_2O_3 modified non-woven separators and a commercial electrolyte was used as they were purchased.

Characterizations

The morphology and microstructure of materials were characterized by SEM (Verios 460 L, FEI). Element distribution was analyzed by SEM-EDS. DSC was performed by a TA DSC 25 calorimeter under a N_2 flow (50 mL/min) at a heating rate of 5 °C/min. TG was conducted at a heating rate of 10 °C/min under a N_2 flow (NETZSCH, 209F3A, Germany). The charge/discharge performance was carried out on an Arbin battery test station (Arbin Instruments, USA).

Safety Performance Tests

Cells with the PE and PET/ceramic non-woven separators were at 100% state of charge. Each cell had a nominal capacity of 42 Ah and the cell voltage was 4.2 V. Nail penetration tests were performed using a 3 mm diameter (nom.) stainless steel blunt rod and the cells were fully penetrated at a rate of 2 cm/s. A thermocouple stick at the center of the cell recorded the surface temperature changes.

Acknowledgements

This work was financially supported by the National Natural Science Foundation of China (U1804255), Tianjin Sci. & Tech. Program (18ZXJMTG00200), the Fundamental Research Funds of Tianjin University of Technology and the Natural Science Foundation of Shandong Province (ZR2017BEM020).

Conflict of Interest

The authors declare no conflict of interest.

Keywords: thermal runaway • nail test • mechanism • coated non-woven separator • lithium-ion battery

- [1] P. Arora, Z. M. Zhang, *Battery separators*, *Chem. Rev.* **2004**, *104*, 4419–4462.
- [2] S. S. Zhang, *J. Power Sources* **2007**, *164*, 351–364.
- [3] X. S. Huang, *J. Solid State Electrochem.* **2011**, *15*, 649–662.
- [4] H. Lee, M. Yanilmaz, O. Toprakci, K. Fu, *Energy Environ. Sci.* **2014**, *7*, 3857–3886.
- [5] J. Xu, L. B. Wang, J. Guan, S. Yin, *Mater. Des.* **2016**, *95*, 319–328.
- [6] C. H. Yuan, L. B. Wang, S. Yin, J. Xu, *J. Power Sources* **2020**, *467*, 228360.
- [7] J. K. Feng, X. P. Ai, Y. L. Cao, H. X. Yang, *J. Power Sources* **2006**, *161*, 545–549.
- [8] C. T. Love, *J. Power Sources* **2011**, *196*, 2905–2912.

- [9] J. Song, M. H. Ryou, B. Son, J. N. Lee, D. J. Lee, J. W. Choi, J. K. Park, *Electrochim. Acta* **2012**, *85*, 524–530.
- [10] B. J. Xiong, R. Chen, F. X. Y. Zeng, J. Kang, Y. F. Men, *J. Membr. Sci.* **2018**, *545*, 213–220.
- [11] T. Yamanaka, Y. Takagishi, Y. Tozuka, T. Yamaue, *J. Power Sources* **2019**, *416*, 132–140.
- [12] D. S. Ren, X. N. Feng, L. G. Lu, X. M. He, M. G. Ouyang, *Appl. Energy* **2019**, *250*, 323–332.
- [13] B. Jung, B. Lee, Y. Jeong, J. Lee, S. R. Yang, H. Kim, M. Park, *J. Power Sources* **2019**, *427*, 271–282.
- [14] T. Wu, K. Wang, M. Xiang, Q. Fu, *Chin. J. Chem.* **2019**, *37*, 1207–1215.
- [15] M. Waqas, S. Ali, C. Feng, D. J. Chen, J. C. Han, W. D. He, *Small* **2019**, *15*, 1901689.
- [16] H. L. Zhang, H. B. Zhao, M. A. Khan, W. W. Zou, J. Q. Xu, L. Zhang, J. J. Zhang, *J. Mater. Chem.* **2018**, *A6*, 20564–20620.
- [17] Y. B. He, Y. Qiao, H. S. Zhou, *Dalton Trans.* **2018**, *47*, 6881–6887.
- [18] B. H. Liu, S. Yin, J. Xu, *Appl. Energy* **2016**, *183*, 278–289.
- [19] B. H. Liu, Y. K. Jia, C. H. Yuan, L. B. Wang, X. Gao, S. Yin, J. Xu, *Energy Storage Mater.* **2020**, *24*, 85–112.
- [20] K. J. Kim, Y. H. Kim, J. H. Song, Y. N. Jo, J. S. Kim, Y. J. Kim, *J. Power Sources* **2010**, *195*, 6075–6080.
- [21] X. S. Huang, *J. Power Sources* **2012**, *216*, 216–221.
- [22] K. Kim, J. Kim, M. Park et al., *J. Power Sources* **2012**, *198*, 298–302.
- [23] X. S. Huang, J. Hitt, *J. Membr. Sci.* **2013**, *425*, 163–168.
- [24] J. D. Li, Q. Zhong, Y. Y. Yao, S. H. Bi, T. Zhou, X. M. Guo, M. Q. Wu, T. T. Feng, R. L. Xiang, *J. Appl. Polym. Sci.* **2018**, *135*, 46508.
- [25] J. C. Liu, K. Yang, Y. D. Mo, S. J. Wang, D. M. Han, M. Xiao, Y. Z. Meng, *J. Power Sources* **2018**, *400*, 502–510.
- [26] J. Liu, Y. B. Liu, W. X. Yang, Q. Ren, F. Y. Li, Z. Huang, *J. Power Sources* **2018**, *396*, 265–275.
- [27] G. F. Zeng, J. Y. Zhao, C. Feng, D. J. Chen, Y. Meng, B. Boateng, N. Lu, W. D. He, *ACS Appl. Mater. Interfaces* **2019**, *11*, 26402–26411.
- [28] M. Kim, G. Y. Han, K. J. Yoon, J. H. Park, *J. Power Sources* **2010**, *195*, 8302–8305.
- [29] X. S. Huang, *J. Power Sources* **2011**, *196*, 8125–8128.
- [30] C. M. Costa, M. M. Silva, S. Lanceros-Mendez, *RSC Adv.* **2013**, *3*, 11404–11417.
- [31] M. Xia, Q. Z. Liu, Z. Zhou, Y. F. Tao, M. F. Li, K. Liu, Z. H. Wu, D. Wang, *J. Power Sources* **2014**, *266*, 29–35.
- [32] Y. Li, H. T. Pu, *J. Power Sources* **2018**, *384*, 408–416.
- [33] W. X. Yang, Y. B. Liu, X. M. Hu, J. B. Yao, Z. J. Chen, M. Hao, W. J. Tian, Z. Huang, F. Y. Li, *Polymer* **2019**, *11*, 1671.
- [34] H. S. Jeong, D. W. Kim, Y. U. Jeong, S. Y. Lee, *J. Power Sources* **2010**, *195*, 6116–6121.
- [35] M. Yanilmaz, Y. Lu, Y. Li, X. W. Zhang, *J. Power Sources* **2015**, *273*, 1114–1119.
- [36] Y. M. Deng, X. N. Song, Z. Ma, X. H. Zhang, D. Shu, J. M. Nan, *Electrochim. Acta* **2016**, *212*, 416–425.
- [37] M. Raja, K. Bicy, S. Suriyakumar, N. Angulakshmi, S. Thomas, A. M. Stephan, *Ionics* **2018**, *24*, 3451–3457.
- [38] W. Na, K. H. Koh, A. S. Lee, S. Cho, B. Ok, S. W. Hwang, J. H. Lee, C. M. Koo, *J. Membr. Sci.* **2019**, *573*, 621–627.
- [39] H. J. Li, L. Li, S. Z. Zheng, X. M. Wang, Z. S. Ma, *Materials* **2019**, *12*, 2813.
- [40] T. H. Cho, M. Tanaka, H. Ohnishi, Y. Kondo, M. Yoshikazu, T. Nakamura, T. Sakai, *J. Power Sources* **2010**, *195*, 4272–4277.
- [41] C. Shi, P. Zhang, S. Huang, X. Y. He, P. T. Yang, D. Z. Wu, D. H. Sun, J. B. Zhao, *J. Power Sources* **2015**, *298*, 158–165.
- [42] X. Liu, D. S. Ren, H. Hsu, X. Feng, G. L. Xu, M. H. Zhuang, H. Gao, L. G. Lu, X. B. Han, Z. Y. Chu, J. Q. Li, X. M. He, K. Amine, M. G. Ouyang, *Joule* **2018**, *2*, 2047–2064.

Manuscript received: July 13, 2020

Revised manuscript received: August 21, 2020

Accepted manuscript online: August 21, 2020

Version of record online: September 29, 2020